

FRACTURE BEHAVIOR AND MECHANICAL CHARACTERIZATION  
OF OBSIDIAN: NATURALLY OCCURRING GLASS

By

MOHAMMED S. HUSIEN

Bachelor of Science in Mechanical Engineering  
Bahir Dar University  
Bahir Dar, Ethiopia  
2004

Submitted to the Faculty of the  
Graduate College of  
Oklahoma State University  
in partial fulfillment of  
the requirements for  
the Degree of  
MASTER OF SCIENCE  
July, 2010

COPYRIGHT ©

By

MOHAMMED S. HUSIEN

July, 2010

FRACTURE BEHAVIOR AND MECHANICAL CHARACTERIZATION  
OF OBSIDIAN: NATURALLY OCCURRING GLASS

Thesis Approved:

Dr. Raman P. Singh

---

Thesis Advisor

Dr. Kaan A. Kalkan

---

Dr. Sandip P. Harimkar

Dr. A. Gordon Emslie

---

Dean of the Graduate College

## ACKNOWLEDGMENTS

Early in the process of completing my master's degree here at Oklahoma State University, it became quite clear that a researcher can not complete his work alone. I would like to thank my research advisor, Dr. Raman P. Singh, who has been a significant presence in my life. His ability to lead is a true gift. I will always be thankful for his wisdom, knowledge, and deep concern not only for me, but also for all MAML colleagues. It has been an honor to work with him.

I would like to thank Dr. Sandip Harimkar and Dr. Kaan Kalkan for being in my thesis committee as well as for pitching in at such a short notice.

I would like to express my gratitude towards my very good friends and lab-mates. I would also like to thank all my friends here at Stillwater whose friendship and affection made Stillwater a home away from home.

Finally, I would like to thank my sister, Fethia, my mother, and all my family for their unconditional love and support without whom I would not have reached this stage!

## TABLE OF CONTENTS

Chapter	Page
<b>1 INTRODUCTION</b>	<b>1</b>
<b>2 EXPERIMENTAL DETAILS</b>	<b>6</b>
<b>3 RESULTS AND DISCUSSION</b>	<b>19</b>
<b>4 CONCLUSIONS AND FUTURE WORK</b>	<b>33</b>
<b>BIBLIOGRAPHY</b>	<b>35</b>

## LIST OF TABLES

Table		Page
3.1	Density of obsidian and reference samples. . . . .	19
3.2	Room temperature thermal conductivity of obsidian determined using the axial heat flow setup. . . . .	21
3.3	Modulus and Poisson's ratio results using pulse-echo . . . . .	22
3.4	Nano-indentation on obsidian and artificial glass . . . . .	28
3.5	Chemical composition of obsidian and soda lime glass wt (%) [53] . . . . .	28
3.6	Comparison of elastic modulus using four different methods . . . . .	29
3.7	Biaxial strength of black, red tiger and fused quartz. . . . .	30
3.8	Values of fracture toughness measured by single edge V notch beam (SEVNB). . . . .	32

## LIST OF FIGURES

Figure	Page
2.1 Three samples of obsidian used in the study black, pink and red tiger from left to right respectively. . . . .	7
2.2 Samples prepared for ring-on-ring (ROR) and conductivity experiment . . .	7
2.3 Samples prepared for Single edge V notch beam . . . . .	8
2.4 Axial heat flow setup for measuring room temperature thermal conductivity [30]. . . . .	9
2.5 Schematic diagram of ultrasonic testing apparatus. . . . .	11
2.6 Ring-on-ring (RoR), flexure schematic. . . . .	14
2.7 Photograph of ring-on-ring (RoR) Fixture. . . . .	15
2.8 Coordinates in vicinity of notch root. . . . .	17
2.9 Sectional view of a diamond wheel specially made for V notch. . . . .	17
3.1 Typical thermocouple data at steady state heat conduction stage. . . . .	20
3.2 The speed of sound of longitudinal and shear wave in obsidian samples . .	22
3.3 XRD-patterns of Black obsidian, red-tiger obsidian and fused quartz. . . . .	23
3.4 X-Ray Fluorescence (XRF) pattern for black obsidian. . . . .	24
3.5 X-Ray Fluorescence (XRF) pattern for red tiger obsidian. . . . .	24
3.6 EDS-Spectrum of red obsidian . . . . .	25
3.7 EDS-Spectrum of Black obsidian . . . . .	25
3.8 Surface SEM images of black and red tiger obsidian . . . . .	26
3.9 Typical load-displacement graph of nano indentation of obsidian . . . . .	27
3.10 Typical ring-on-ring (RoR) failure of black, red tiger and fused quartz. . . .	30

3.11 Typical load-deflection curve of obsidian under ring-on-ring (RoR). . . . .	30
3.12 Scanning electron microscope(SEM) images of fracture surfaces of black and red tiger obsidian . . . . .	31

## CHAPTER 1

### INTRODUCTION

#### **Objective**

The objective of this work is to investigate the mechanical properties and fracture behavior of three types of obsidians, namely black (B), pink (P), and red tiger (RT) in comparison with reference materials.

Volcanic obsidian has several unique properties that makes it the ideal archaeological material for studying prehistoric trade and exchange. The sourcing of archaeological obsidian can be of great assistance for investigating the cultural, social, and economic development of ancient societies. As a result, several people investigated the elemental compositions to determine the source of archeological obsidian. Nevertheless, it is a strange fact that from over thousand publications on obsidian only few have been concerned with the mechanical properties of this natural glass. This is despite the fact that this material gained importance in pre-historic times specifically due to its mechanical properties. Studying the unique mechanics and structural features of volcanic glass will help in distinguishing the micro fracture behavior of obsidian versus artificial glasses and fused quartz. Furthermore, it will also help provide a basis for microstructural design of artificial glass with increased toughness.

#### **Background**

Obsidian is a naturally occurring glass formed as an extrusive igneous rock [1–7]. It is a supercooled liquid that formed when highly viscous volcanic lava of high silicon and aluminum content cools rapidly. The speed at which it cools prevents crystallization and the

rock forms as solid volcanic glass. The glass is generally black or gray in color. Obsidian can also be found in light brown, brown mottled with black, and black with a beautiful golden or silvery sheen (other colors are possible, depending upon the composition and the circumstances of formation), and it is sometimes banded or streaky in appearance [2]. Snowflake obsidian is dotted with white patches where parts of the rock have begun to crystallize. Obsidian is physically amorphous and isotropic which is due to its entirely disordered atomic structure. This is one of the main reasons why it makes such efficient tools, since flakes can be struck from a core in almost any direction.

Natural glass is not a stable material at ambient temperatures and pressures; it slowly hydrates through the diffusion of water into the outer surface and along cracks to form perlite. As a result, by geological standards its lifetime is relatively short. The sources of obsidian exploited by prehistoric peoples are almost entirely restricted to young volcanic areas. Few obsidian sources are greater than 10 million years old, and many are less than 100,000 years of age [8]. Geographically, obsidian sources are found in areas which have experienced rhyolitic eruption. The Mediterranean, the Andes Mountains of South America, Central Europe, Turkey, Eastern Africa, the western United States and Alaska, the trans-Mexican volcanic belt, Japan, New Zealand, and the islands of the South Pacific are the most common areas where obsidian can be found [9]. The Western U.S. include Arizona, Colorado, New Mexico, Texas, Utah, Washington and Idaho.

In early times, obsidian was used in different places for a variety of applications. It has been used since prehistoric times for making tools, masks, weapons, mirrors, and jewelry. In the Maya highlands, obsidian was available to all households and it was found in everyday situations such as hunting and agriculture [10]. Knives, lance and dart points, prismatic blades are some examples of obsidian tools used in Maya. These tools were sometimes used for woodworking or shaving, bone working tools, bifacial, retouched flakes, and spearheads for warfare. When skillfully worked, the material can be used to make some of the sharpest edges on earth. Due to this the practical use of obsidian is obvious. The edges of prismatic

blade prepared from obsidian can reach the molecular level. There are a large number of blades made from obsidian and believed to have a cutting edge that is only one molecule thick. In some parts of the world such as North America and South America, obsidian was used as healing for different diseases. It was believed to reduce tension and depression, and release emotions. It was also used to clear unconscious blocks and detachment with wisdom and love [9].

The chemical composition of obsidian has been investigated in many papers that suggest that it is rich in silica [11–15]. Obsidian has water content that ranges from 0.1 to 0.5%. When exposed to groundwater it progressively hydrated, forming perlite. Due to this hydration, the water content of obsidian increases to about 5 wt %. The increase in the water content results in cracking patterns that gradually destroy the glass. There are trace elements present in obsidian at concentrations below 1% [8]. The chemical property of obsidian is homogeneous in most obsidian sources, with variations in composition on the order of a few percent or less. On the other hand, different sources have different compositions. The compositions of parent rocks that were melted and changes that take place in the magma chamber before eruption reflect these changes in the composition. The abundance of trace elements by an order of magnitude suggests that the variations within sources are smaller.

### **Literature Survey**

Investigations on determining the origin of archaeological obsidians have become a normal part of prehistoric studies since the 1970s. The provenance of obsidian artifacts have been successfully established by studies made by different scholars. Some researchers focus on chemical characterization as way to source obsidian and reconstruct patterns of distribution and exchange. In addition, there are some studies that use obsidian hydration as a chronometric method [16–18].

In Southern America, identifying the elemental composition of obsidians helped many

researchers to study the provenance [12, 17]. Fission track (FT) dating is another method used to determine the source of archaeological obsidians. This method studies their formation age. Certain provenance studies used both FT dating of obsidian artefacts and elemental compositions, as determined by particle induced X-ray emission (PIXE) [8, 16, 18]. It also appeared that samples presenting the same elemental composition might present differences in formation ages [19–24].

Over the past few decades, the characterization of archaeological materials to support provenance research has grown rapidly [8, 20]. There are quite unique properties that make volcanic obsidian essential for studying prehistoric trade and exchange. Obsidian lava is formed when it is in equilibrium with solid materials at high temperatures, which is approximately greater than 1000°C . During this process, the trace elements are distributed between the liquids and solids. Transition elements such as cobalt, chromium, and nickel are strongly absorbed by the solids. These elements are compatible with the crystallization of solids and readily removed from the liquid phase. That is why they are known as the compatible elements. There are other elements which are incompatible with the solid phase and they tend to become more concentrated in the liquid. This incompatibility of elements with the solid phase is caused by two factors. The first cause of incompatibility may be that ions such as rubidium, barium, strontium, and cesium are too large for the available ionic sites in the solid. Second, certain ions have too high a charge to fit within the crystal structure of the solid. Examples of the latter include quintuply charged ions such as niobium and tantalum, the quadruply charged ions of hafnium, thorium, and zirconium or the triply charged rare earths such as cerium and lanthanum [27, 28]. Consequently, the incompatible element mixtures may differ from one source to the next and become a sensitive indicator of origin. It also is possible within a single magma chamber, as the magma evolves, that glass eruptions occurring at different times will have different trace element chemistries [1].

Dorfman *et al.* studied the mechanical properties of 15 kinds of obsidian. This study focuses on the mechanical and structural analysis of obsidian by micro and nano-indentation,

XRD, SEM, and TEM. They concluded that, the micro-mechanical features of obsidian reveals its strongly distinctive behavior vs various kinds of artificial glass including lime glass and fused quartz [25].

## CHAPTER 2

### EXPERIMENTAL DETAILS

#### Origin and Preparation of Studied Samples

Three samples of obsidian were evaluated in comparison with the reference material. Davis Creek, California was the source for black and pink obsidians. The red tiger obsidian was from Glass Butte, Oregon. The bulk black obsidian was uniform jet-black color, and the red tiger and pink obsidians consist of at least two different-colored areas as shown in Fig. 2.1; one area jet-black in color just as black obsidian and another area red or brown in color. In contrast, all of the reference materials were colorless and optically clear.

Ericson *et al.* used 28 rhyolitic obsidian samples from California, Western Nevada and Southern Oregon, to study their chemical and physical properties [1]. They determined the mean chemical compositions of these samples as, 79.26% SiO<sub>2</sub>, 4.14% Na<sub>2</sub>O, 0.35% CaO, 12.41% Al<sub>2</sub>O<sub>3</sub>, 3.98% K<sub>2</sub>O, 1.47% Fe<sub>2</sub>O<sub>3</sub>, 0.05% MgO, and 0.11% TiO<sub>2</sub>, which is the same as the material used in this study. These results show that rhyolitic obsidian is a high alumina glass with similar chemical composition to that of normal granites and rhyolitic rocks. Based on the small standard deviations of each oxide the major chemical composition of rhyolitic obsidian is relatively invariant.

The black and red tiger obsidian samples used in this research were acquired from Wards Natural Science Establishment (Rochester, NY). Some samples of black, red tiger and, pink obsidian were also available from prior research [25]. General purpose glass which used as a glass slide with similar silica composition was used as a reference material. This glass commonly referred to as Type II Soda Lime Glass per A.S.T.M.- 438 federal spec DD-G-54lb. The chemical composition of this lime glass is given as, 73% SiO<sub>2</sub>, 14%



Figure 2.1: Three samples of obsidian used in the study black, pink and red tiger from left to right respectively.

$\text{Na}_2\text{O}$ , 7%  $\text{CaO}$ , 4%  $\text{MgO}$ , and 2%  $\text{Al}_2\text{O}_3$ . The other reference material used was fused quartz with the chemical composition given as, 75.94%  $\text{SiO}_2$ , 0.7%  $\text{Na}_2\text{O}$ , 0.4%  $\text{CaO}$ , 0.1%  $\text{MgO}$ , 14%  $\text{Al}_2\text{O}_3$ , 0.6%  $\text{K}_2\text{O}$ , 0.2%  $\text{Fe}_2\text{O}_3$ , 1.1%  $\text{TiO}_2$ , and 0.8%  $\text{ZrO}_2$ . The soda lime glass and the fused quartz were acquired from Ted Pella. Inc. (Redding, CA).

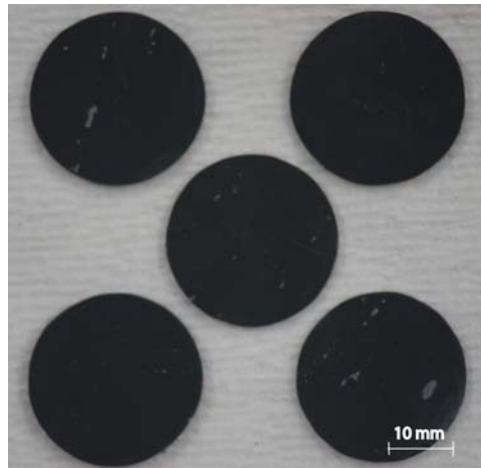


Figure 2.2: Samples prepared for ring-on-ring (ROR) and conductivity experiment

Figure 2.2 shows samples prepared for ring-on-ring experiments. The size of the samples received from Ward's were much bigger than that were needed for the experiment. Therefore, they were cut using a high-speed diamond saw and polished to obtain an acceptable finish. These samples were approximately  $\phi 25 \times 1.5\text{mm}$ . The cylindrical samples shown in Fig. 2.2 were also used to measure thermal conductivity by using the axial flow method. For nano-indentation testing, the obsidian samples were cut in to flat 0.5-inch

thick slices with a diamond-impregnated cutting wheel and they were mounted in epoxy and polished to obtain mirror finish using standard metallographic preparation techniques. Rectangular specimens,  $3 \times 4 \times 40$  mm in dimension, were prepared for single edge V notch beam (SEVNB), as shown in the Fig. 2.3. The samples were prepared keeping all the faces parallel, which made the sample preparation tedious and time taking. Advanced machining techniques and a V-shaped diamond wheel had to be developed for this specimen. This wheel was obtained from UKAM Industrial Superhard Tools (Valencia, CA).



Figure 2.3: Samples prepared for Single edge V notch beam

### Density Measurements

The density of obsidian samples was determined using the buoyancy method. In this study, first the specimen was dried at  $100^{\circ}\text{C}$  for 24 hours, until it reached a constant mass, and this dry mass of the sample,  $m_1$ , was recorded. Subsequently, the apparent mass of the sample immersed in water,  $m_2$ , was determined using a density determination kit (Sartorius YDK 01, Sartorius AG, Goettingen, Germany). The density of the liquid causing buoyancy depends on its temperature. Thus, the temperature of water was also recorded to correct for variations in the density,  $\rho_{fl}$ , as a function of temperature. Finally, the bulk density,  $\rho_b$ , was calculated as,

$$\rho_b = \frac{m_1}{m_1 - m_2} \rho_{fl}, \quad (2.1)$$

## Thermal conductivity

Thermal conductivity,  $\lambda$ , is a measure of the heat flux that flows through the material for a certain temperature gradient. It depends on various factors including crystal plane structure, surrounding temperature, phase, and form. The thermal conductivity of obsidian was characterized using a steady state axial flow setup, shown in Fig. 2.4. The obsidian samples were prepared in cylindrical shape with the dimension  $\phi 25 \times 1.5$  mm. Eight T-type thermocouples located in the hot and cold side of the sample (mounted on copper rods) were used to measure the heat flow. In order to prevent the heat loss from the setup through conduction in the radial direction, thick teflon cylinder insulation was used. The cold side temperature was controlled using an analog controlled Cole Palmer chiller, model:12750-00 (Cole-Parmer, Vernon Hills, IL) and the hot side using Omega CN132 temperature/process controller (Omega Engineering, Inc., Stamford, CN). Data was recorded using a Fluke 53 series II digital storage thermometer (Fluke Corporation, Everett, WA), after steady state conditions had been achieved in  $\approx 24$  hours.



Figure 2.4: Axial heat flow setup for measuring room temperature thermal conductivity [30].

## Elastic Constants Using Pulse-Echo Method

Ultrasound is mostly used to determine material characteristics of interest such as the presence of voids, cracks, porosity, part thickness, and weld penetration [31–33]. It uses very high frequency sound, higher than 20 kHz. In this experiment, the Young’s modulus and Poisson’s ratio for all types of obsidians and the reference materials were determined by measuring wave speeds. The speed of sound in these solids was measured by using the pulse-echo technique [34]. This technique is simple, quick, and accurate method of measuring the speed of sound in solids.

The pulse-echo technique, as shown Fig. 2.5, uses an ultrasound transducer that generates an ultrasonic pulse and receives its “echo”. This transducer acts as both transmitter and receiver in one unit. The transducer broadcasts the ultrasonic pulse at the surface of the specimen which travels through the specimen and reflects off the opposite face. The ultrasonic pulse keeps bouncing off the opposite faces of the specimen, attenuating with time. Measuring the length between any two echoes one can calculate the speed of sound in a solid, as per Eqn. 2.2.

$$C = \frac{2d}{\Delta t} \quad (2.2)$$

where,  $\Delta t$  is round trip transit time and  $d$  the measured thickness of the specimen. It may be shown that the speed of sound of longitudinal and shear waves is given by:

$$C_L = \sqrt{\frac{E(1 - \nu)}{\rho(1 + \nu)(1 - 2\nu)}} \quad (2.3)$$

$$C_s = \sqrt{\frac{E}{\rho 2(1 + \nu)}} = \sqrt{\frac{G}{\rho}} \quad (2.4)$$

where  $E$  is Young’s modulus (or the modulus of elasticity),  $\nu$  is Poisson’s ratio, and  $G$  is the shear modulus. Solving these equations for  $E$  give:

$$E = 2\rho C_s^2(1 + \nu) \quad (2.5)$$

Thus, given measurements of  $\rho$ ,  $C_L$ , and  $C_s$ , it is possible to determine  $E$  and  $\nu$ .

Direct contact transducers such as 10 MHz longitudinal wave transducer and 5 MHz shear wave transducer was used to broadcast the ultrasonic pulse. A digital storage oscilloscope was also used to measure the time between the first echo and the second echo. While measuring the speed of the waves, coupling agents was used between the contact transducer and the specimen.

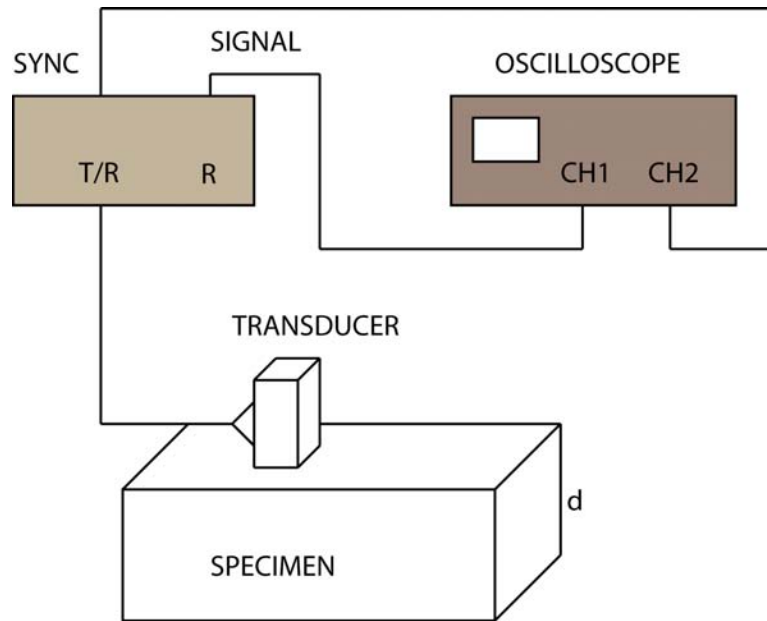


Figure 2.5: Schematic diagram of ultrasonic testing apparatus.

### **X-ray Diffraction**

X-ray diffraction (XRD) is a tool for identifying, quantifying and characterizing the fine structure of matter [36]. In this study, Bruker D8 discover diffractometer (Bruker AXS Inc., Madison, WI ) was used to identify the patterns of black and red tiger obsidian and compare it with fused quartz. This patterns helped to distinguish crystalline materials from amorphous ones.

## **X-Ray Fluorescence**

In the mid-20th century, the emergence of instrumental methods such as neutron activation analysis, emission spectroscopy and X-ray fluorescence (XRF) spectrometry increased studies on stone tools, pottery, and other archaeological specimens. In particular, XRF has been employed most often for the analysis of obsidian artifacts in the Americas. A portable X-ray fluorescence (RACeR III-V, Bruker AXS Inc., Madison, WI ) instrument was used to analyze the three types obsidians. Settings that allow all the x rays from 17 keV to 40 keV to reach the sample were allowed, thus efficiently exciting the elements from Fe to Mo.

## **SEM/EDS Analysis**

SEM (scanning electron microscope) can be utilized for high magnification imaging of almost all materials. In this study Hitachi S-4800 Type II Ultra-High resolution field emission scanning electron microscope (GCeMarket, Inc., Blackwood, NJ) was used. With SEM in combination of EDS (Energy dispersive X-ray spectroscopy) it is also possible to determine which element is present in different parts of the sample. In this research the analyses of sample chemistry were carried out by means of the same SEM facility using an EDS system. The SEM-EDS microanalyses were carried out on the relatively flat surface of small obsidian. Since the accuracy EDS spectrum can be affected by the nature of the sample, the obsidian samples were polished.

## **Nano-indentation**

Nano-indentation is a useful technique for determining the mechanical properties of small structural features and thin films [25]. Elastic modulus,  $E$ , and hardness,  $H$ , are the two mechanical properties measured most frequently using load and depth sensing indentation techniques [37–39]. For nano-indentation testing, samples were cut using a high-speed diamond saw, mounted in epoxy and then polished to obtain a mirror finish. Indentation was done on MTS Nano Indenter XP (MTS Systems Corporation, Oak Ridge, TN, USA) using

a Berkovich indenter, and the analysis of indentation data was performed using the accompanying software TestWorks4 (MTS Systems Corporation). Experiments were performed in load-controlled mode and a peak load of 30 mN was used. The methods for determining the elastic modulus and hardness have become fairly standard and are based on the fact that the displacements recovered during unloading are largely elastic. The program determines the elastic modulus from the unloading part of the load displacement data and uses the method developed by Oliver and Pharr to determine the projected contact area and hence the hardness of the material [38]. For the sake of analysis, the Poissons ratio of obsidian was assumed to be the same as that for lime glass.

### **Biaxial Flexure Strength**

Biaxial flexure test methods are preferred over uniaxial testing for characterization of ceramics. The strength of ceramic materials depend on the stressed area and the statistical distribution of strength-controlling three dimensional flaws. Therefore, the test must be designed such that the maximum area is tested to minimize sampling error. The benefits of biaxial flexure tests include the examination of a large surface area that is free from edge finishing defects, ease of test piece preparation, and the applicability of this method to thin sheets. A larger stressed area increases the probability of characterizing the flaw population successfully. In uniaxial tests, failure is governed by the condition of edges parallel to the major axis. This may result in improper judgement of the material strength and behavior. This makes the biaxial stress distribution, where the stress is maximum over a plane, more discriminate of material defects than a uniaxial distribution. In the biaxial flexure test method the maximum tensile stress occurs within the central loading area, far from edges, and spurious edge failures are eliminated [30].

The ring-on-ring (RoR) configuration is one of the biaxial tests that exposes the maximum area under a constant maximum stress. The RoR is an axisymmetric test, where the disc is supported by a ring and loaded from the opposite side by another smaller concentric

ring, as shown in Fig. 2.6. In general, there is no strict shape requirement for the test sample as long as the outer perimeter is known. This configuration subjects a greater portion of the specimen to an equibiaxial stress state and distributes the applied contact load over a larger area compared to any other biaxial test methods. The concentric support ring in RoR configuration reduces the likelihood of fixture-induced specimen failure leading to invalid test data [42].

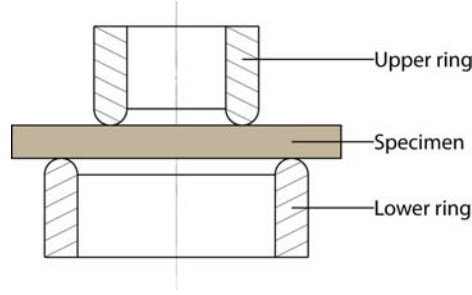


Figure 2.6: Ring-on-ring (RoR), flexure schematic.

For a ring-on-ring test, the radial ( $\sigma_r$ ) and the tangential ( $\sigma_t$ ) stresses within the smaller ring are equal and is given by Eqn. 2.6,

$$\sigma_{\text{RoR}} = \frac{3P}{4\pi t^2} \left[ \frac{(1-\nu)(a^2-b^2)}{a^2} \frac{a^2}{R^2} + 2(1+\nu) \ln \frac{a}{b} \right] \quad (2.6)$$

where  $P$  is the applied load,  $\nu$  is the Poisson ratio of the specimen and was assumed to be 0.20 for SiC,  $a$  is the radius of the support ring,  $b$  is the radius of the load ring, and  $R$  and  $t$  are the radius and thickness of the disc specimen, respectively. A correction factor,  $a^2/R^2$ , is commonly used to accommodate the stiffening effect due to the overhang. The radial ( $\sigma_r$ ) and the tangential ( $\sigma_t$ ) stresses outside the inner ring,  $b \leq r \leq a$ , are given by the expressions given below:

$$\sigma_r = \frac{3P}{4\pi t^2} \left[ 2(1+\nu) \ln \frac{a}{r} + \frac{(1-\nu)b^2(a^2-r^2)}{a^2 r^2} \frac{a^2}{R^2} \right] \quad (2.7)$$

$$\sigma_t = \frac{3P}{4\pi t^2} \left[ 2(1+\nu) \ln \frac{a}{r} - \frac{(1-\nu)b^2(a^2-r^2)}{a^2 r^2} \frac{a^2}{R^2} + 2(1-\nu) \frac{a^2}{R^2} \right]. \quad (2.8)$$

It can also be noted that the stresses are independent of the Young's modulus of either the test material or the rings, but rather depend on the Poisson's ratio of the disc.

Care is needed to select the diameters of the loading and support rings, relative to the specimen thickness, in order to promote a valid failure event. Clean loading conditions and plane-parallel disk shaped specimens are required for the RoR configuration. Lack of these conditions may result in a 3-point contact between ring and specimen. If the contact stresses are large, the measured stresses deviate from the theoretical model and the failure is biased at the contact location. Therefore a ring crosssection radius of  $t/4$  to  $3t/4$ , reduces the elevation in the tensile stresses to less than 2% [34]. The concentric rings in the current setup were made up of stainless steel and had bullnose edges with a radius of 0.3125 mm towards the loading side. This configuration employed a support ring diameter of 19.05 mm and the loading ring diameter of 6.35 mm.

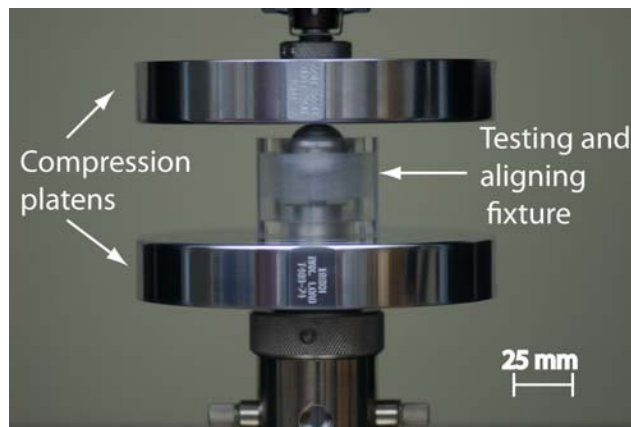


Figure 2.7: Photograph of ring-on-ring (RoR) Fixture.

The specimens were loaded in the RoR fixture using a table-top test frame (Instron<sup>®</sup> 5567, Instron Corporation, Norwood, Massachusetts, USA) as shown in Fig. 2.7. Adhesive tape was applied as per ASTM C1499-05 on the compressive side of the sample which reduced stress concentration and helped in retaining the disc fragments together after the failure. Displacement controlled loading at a rate of 0.5 mm/min was used and the load versus load-point displacement was recorded till the point of failure. Then the flexural

strength was calculated from the peak load sustained by the specimen. A minimum of five samples were tested for each material. The flexure strength was then determined as per Eqn. 2.6, using the peak load at failure.

## Fracture Testing

One of the primary areas of focus of this investigation was the determination of the fracture toughness of obsidian. Due to its simple concept, simple procedure and applicability to a wide variety of materials, single edge precracked beam (SEPB) is a reliable technique for evaluating fracture toughness of ceramics. It involves creation of a straight-through crack from an indentation crack. The difficulty to induce the precrack in some ceramics and the visibility of the crack front, however, are the major draw backs. In this study, the SEPB method was combined with the V notch technique for fracture toughness measurements. Single edge V notched beam (SEVNB) was proposed by Hideo Awaji *et al.* [46]. It is an improved versions of the SEPB, but it requires a sharp V shaped notch with very small root curvature. To get a very sharp notch, advanced machining techniques and V-shaped diamond wheel had to be developed.

It is well established by the linear elastic fracture mechanics that the stress distribution around a crack tip has a square root singularity and is exactly characterized by the stress intensity factor. As for a finite plate with a V notch under tension, it is known that the distribution keeps the inverse square root property when the notch angle is below 30° [46]. Then the stress distribution around a V notch is also characterized by the stress intensity factor explicitly [48]. A notch with finite root radius has no stress singularity at the tip. However, the stress distribution around the tip can be expressed by the stress intensity factor in the same way as a crack tip.

$$\sigma_{y,n} = \frac{k_{1,n}}{(2\pi r^{\frac{1}{2}})} \frac{1 + \frac{\rho}{r}}{1 + \frac{\rho^{\frac{3}{2}}}{2r^{\frac{3}{2}}}} \quad (2.9)$$

where  $k_{1,n}$ , is the stress intensity factor for a notch,  $\rho$  is the root radius and  $r$  is the distance from the notch tip, as shown in Fig. 2.8. It is expected that the fracture toughness

would be evaluated precisely by a V shaped notch of very sharp root radius with the included angle below  $30^\circ$ , based on an assumption that unstable crack propagation initiates in a similar manner to that for a sharp precrack.

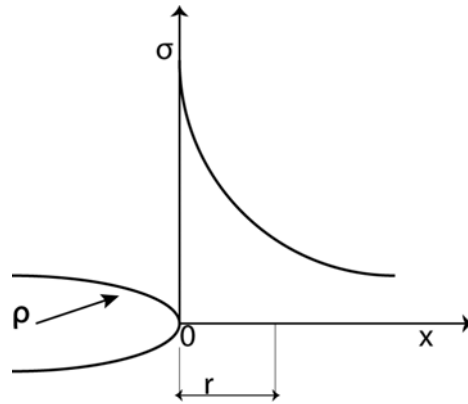


Figure 2.8: Coordinates in vicinity of notch root.

A specially formed diamond slicing wheel was developed for the purpose of machining the above mentioned V notch, of which a sectional view is shown in Fig. 2.9. The bonding material of this wheel was metal, the diamond grit size under  $12/25 \mu\text{m}$  (1000 mesh) and the concentration 100 ( $4-4 \frac{\text{carats}}{\text{cm}^3}$ ). This wheel was produced by UKAM Industrial Superhard Tools Industrial Co. Ltd (Valencia, CA). The machine used for machining the V notch was slow speed precision cutting machine. Testing was carried out in a full size specimen with a geometry of  $3 \times 4 \times 40 \text{ mm}$ . Here, three-point flexure was employed by taking the support span as 30 mm. Equation 2.11 was used to find the shape factor and equation 2.10 is suitable for the stress intensity coefficient as suggested by Awaji *et al.* [46]

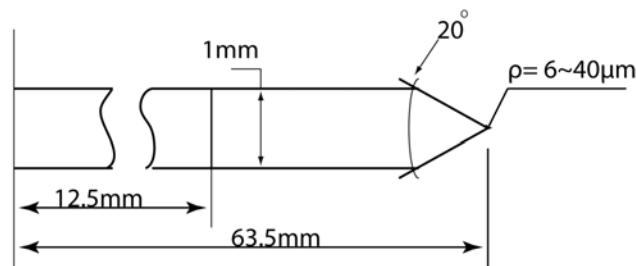


Figure 2.9: Sectional view of a diamond wheel specially made for V notch.

$$K_1 = \frac{3PS}{2B(W)^2} a^{\frac{1}{2}} Y \quad (2.10)$$

$$Y = 1.964 - 2.837\alpha + 11.711\alpha^2 - 23.25\alpha^3 + 24.129\alpha^4 \quad (2.11)$$

$$\alpha = \frac{a}{W} \quad (2.12)$$

where  $P$  is the maximum fracture load,  $S$  the span,  $B$  the specimen thickness,  $W$  the specimen width,  $a$  the precrack length, and  $Y$  the coefficient of the shape factor.

## CHAPTER 3

### RESULTS AND DISCUSSION

#### Analytical and Physical Characterization

Densities of black, pink, and red tiger obsidian samples were measured. About ten test samples were taken from each type of obsidian. The bulk densities of the obsidians are listed in Table 3.1. They ranged from 2.22 to 2.46 g/cm<sup>3</sup> with the mean being  $2.37 \pm 0.02$ . There was a very small difference in the density of the three obsidians, which was within a range of  $\pm 1\%$ . This density differences was not only caused by the chemical composition but also by the thermal history the glass suffered during geological times. Here, reheating events may have played an important role in the history of the obsidian lava flow [24]. The density of soda lime glass and the fused quartz listed in Table 3.1 were acquired from data sheet of Ted Pella. Inc. (Redding, CA).

<b>Material</b>	<b>Bulk density</b> $\rho_b$ (g/cm <sup>3</sup> )
Black obsidian	2.31±0.05
Pink obsidian	2.22±0.07
Red tiger obsidian	2.45±0.06
Fused quartz	2.2
Soda lime glass	2.4

Table 3.1: Density of obsidian and reference samples.

Figure 3.1 shows a typical data set that was recorded by using a steady state axial flow

setup to measure thermal conductivity, as discussed in previous chapter. Two batches of obsidian samples were tested over a period of  $\approx 24$  hours to get constant slope, with each batch consisting of at least ten samples. The hot and cold side linear curves were extrapolated to determine the temperatures,  $T_{hot}$  and  $T_{cold}$ , at the specimen interfaces [51]. Equation 3.1 was used to calculate the heat flow,  $Q$ , on both sides of the specimen, represented as  $Q_{hot}$  and  $Q_{cold}$ . Subsequently, the thermal conductivity, of the sample was determined using the Fourier law of heat conduction, as given in Eqn. 3.2. The room temperature thermal conductivity of red tiger and black obsidian is given in Table 3.2. The measured values of thermal conductivity for obsidians at atmospheric pressure are compared with the recommended values from the literature. These values were found to be almost similar for both obsidians and lower than the literature values of fused quartz [50].

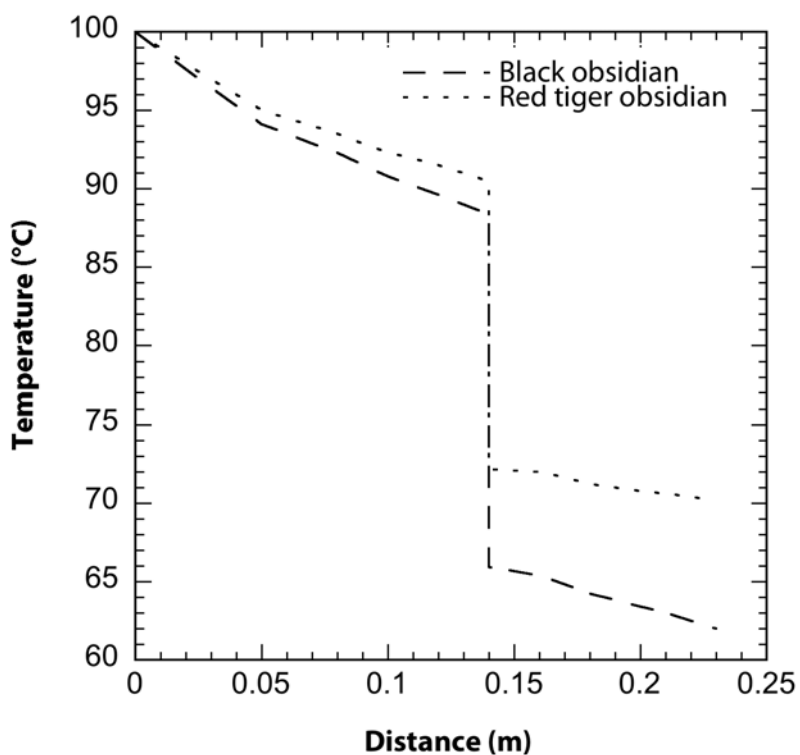


Figure 3.1: Typical thermocouple data at steady state heat conduction stage.

$$Q = -\lambda A \left( \frac{\Delta T}{\Delta Z} \right) \quad (3.1)$$

$$\lambda_{sample} = \frac{(Q_{hot} + Q_{cold})L_{sample}}{2A_{sample}(T_{hot} - T_{cold})} \quad (3.2)$$

<b>Material</b>	<b>Thermal Conductivity</b>
	(W/m-K)
Black obsidian	1.06
Red tiger obsidian	0.96
Fused quartz	1.28
Soda lime glass	0.97

Table 3.2: Room temperature thermal conductivity of obsidian determined using the axial heat flow setup.

Figure 3.2 shows a train of sound wave echoes from multiple round-trips through the specimen. Accurate measurement of the time between the first echo and the second echo was taken from these figures displayed on the oscilloscope. Figure 3.2 shows all the obsidians exhibit no significant variations in sound velocity from point to point and also from sample to sample. This property is typical in homogeneous materials. Values for the speed of sound in these solids range from 1 to 8 km/s, which is the standard range. The stress wave speeds were used to calculate the elastic moduli,  $E$ , and Poisson's ratio,  $\nu$ . The elastic modulus values of obsidian listed in Table 3.3 are higher than the soda lime glass. It might be because of the open spaces present in the structure of the glass, since elastic modulus is derived from the elastic property of the glass structure.

Figure 3.3 shows the XRD-patterns of black obsidian, red-tiger obsidian, and fused quartz. We can see from the diagram that, no sharp peaks are present. This was expected because the obsidians tested were amorphous, and amorphous or poorly crystalline materials does not contribute to diffraction peaks. The broad XRD peaks in the range from  $10^\circ$

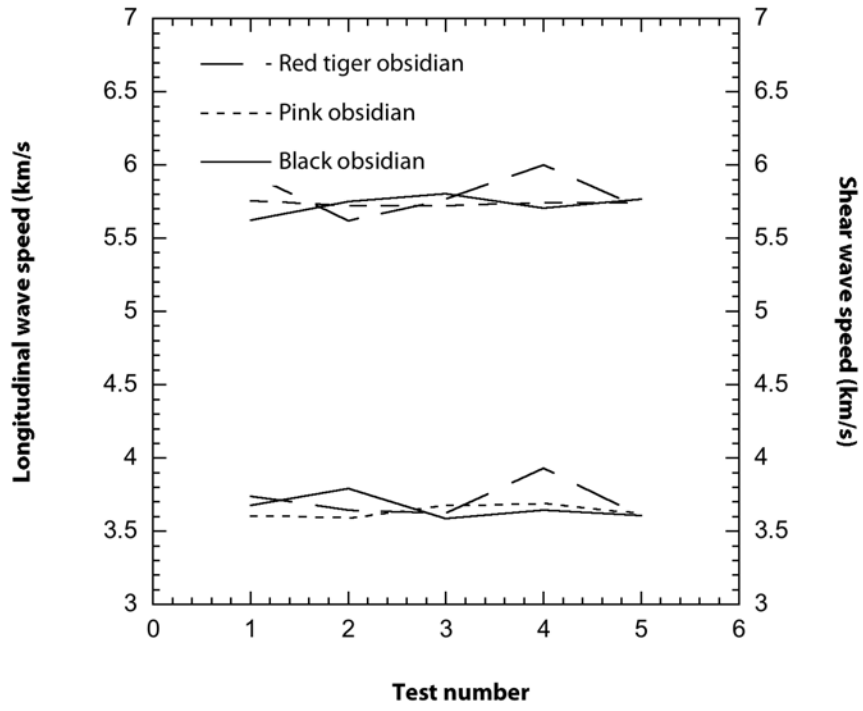


Figure 3.2: The speed of sound of longitudinal and shear wave in obsidian samples

Material	Modulus (GPa)	Poisson's ratio)
Black obsidian	$65.35 \pm 1.6$	$0.18 \pm 0.01$
Red tiger obsidian	$69.12 \pm 4.3$	$0.17 \pm 0.03$
Pink obsidian	$67.46 \pm 3.2$	$0.19 \pm 0.03$
Soda lime glass	$52.87 \pm 2.7$	$0.2 \pm 0.2$

Table 3.3: Modulus and Poisson's ratio results using pulse-echo

to 40° are also indicative of a typical amorphous matrix signature. For reference, the XRD patterns of the fused quartz is also exhibited in Figure 3.3.

As shown in the Figs. 3.4 and 3.5, the X-ray fluorescence measurement shows the presence of Si, Fe, K, Ar, Ni, Cu, Sn and Ru elements and very small amount of P and Ag. This elements are common in volcanic glass. It also seen in the patterns that all types of obsidians exhibit similar elements with significant amount of silicon.

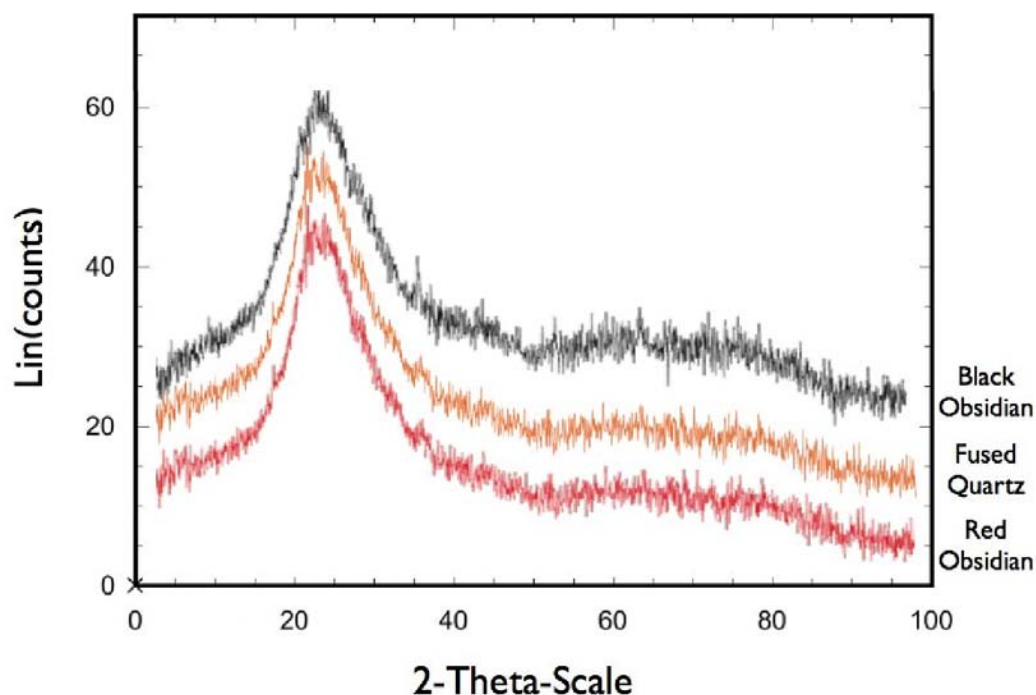


Figure 3.3: XRD-patterns of Black obsidian, red-tiger obsidian and fused quartz.

Obsidian specimens were coated with gold for SEM imaging and EDS analysis. Figures 3.6 and 3.7 display comparable overall EDS spectra, which were collected from obsidians. The black, red tiger and pink obsidians have similar overall EDS spectra and similar concentration levels of the bulk elements such as O, Si, Al, Na, and K. As shown in fig. 3.7, there is a vary small amount of Fe seen in EDS spectrum which might be the result of the dark color from black obsidian.

Figure 3.8 shows SEM images of black and red tiger obsidian. In the present study, the grain surface of obsidian showed the presence of curved structure which is very small in

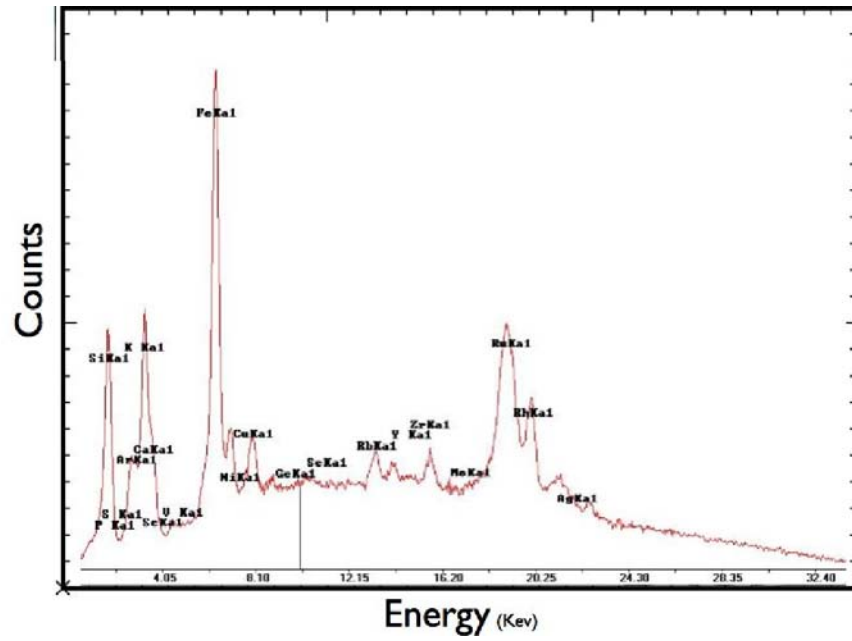


Figure 3.4: X-Ray Fluorescence (XRF) pattern for black obsidian.

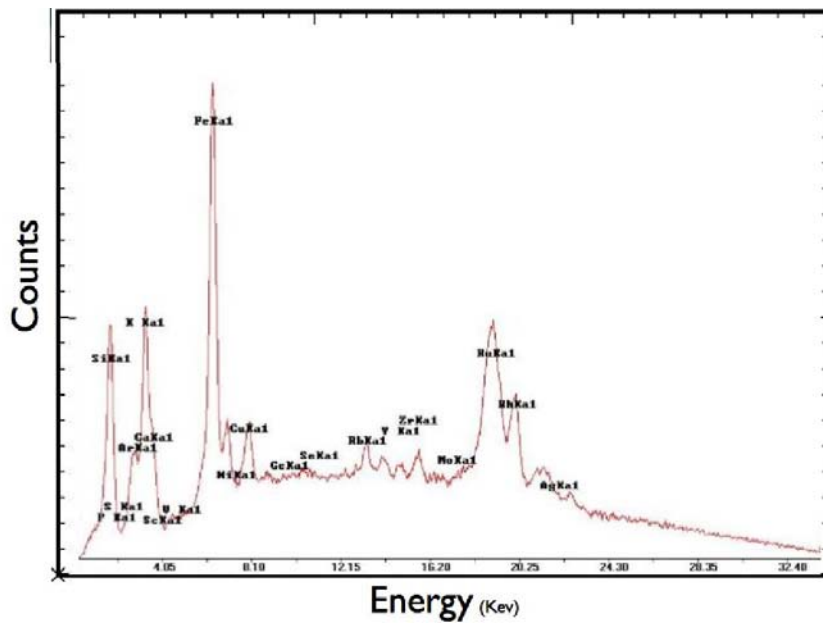


Figure 3.5: X-Ray Fluorescence (XRF) pattern for red tiger obsidian.

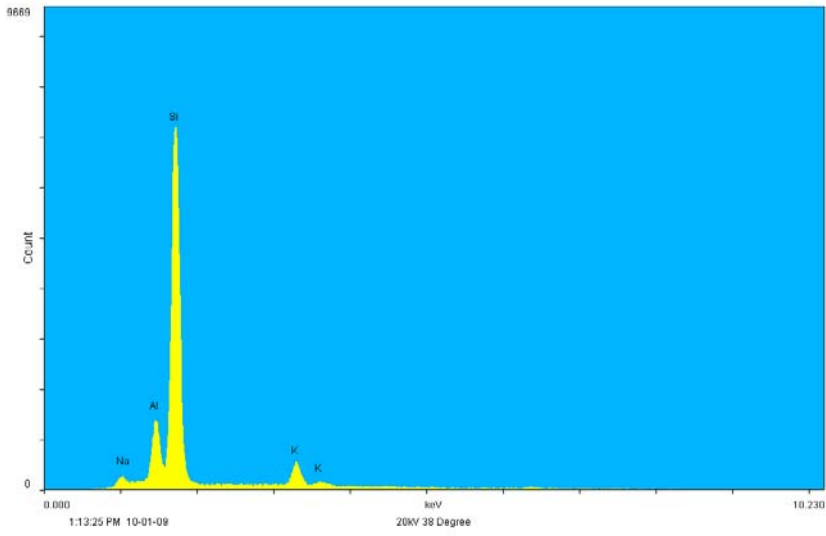


Figure 3.6: EDS-Spectrum of red obsidian

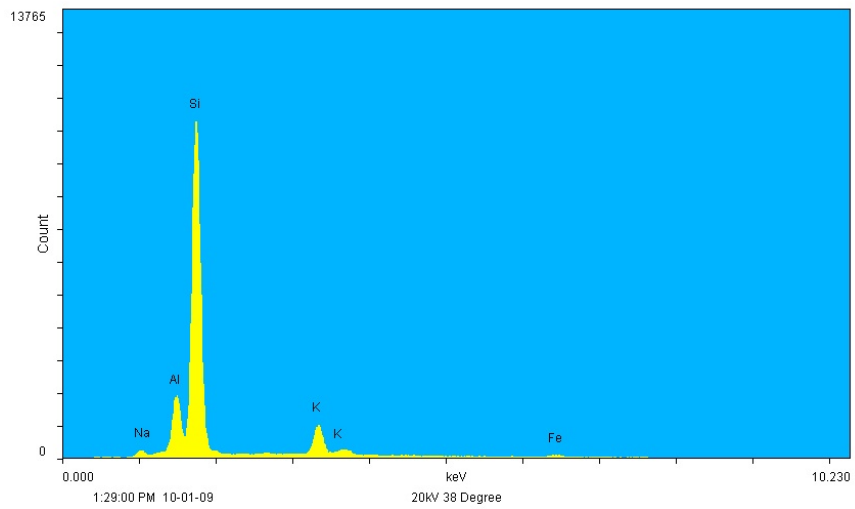
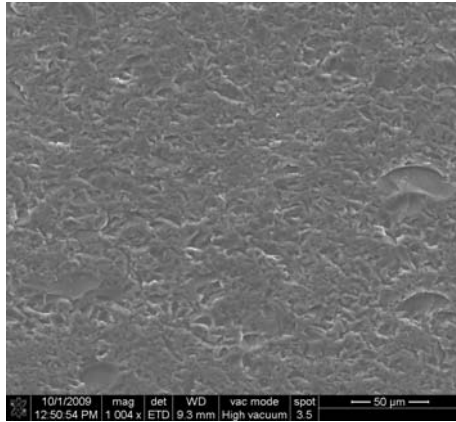
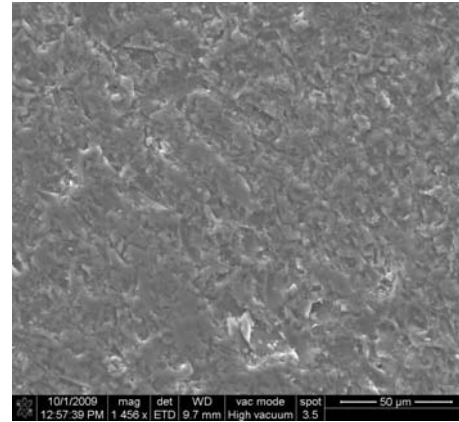


Figure 3.7: EDS-Spectrum of Black obsidian

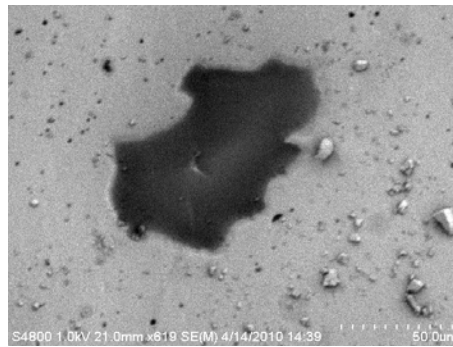
size. Figure 3.8(b) from the black obsidian clearly displays that, the gray-contrast domains usually display feather-like or snowflake-like shapes. Figure 3.8(a) from the red tiger is similar to Fig. 3.8(b), but the small inclusions are irregular. Figure 3.8(c) also indicates there are some pores present in the surface of obsidian in addition to tiny swellings.



(a) SEM images of red tiger obsidian



(b) SEM images of black obsidian



(c) SEM image showing some pores in the surface of obsidian

Figure 3.8: Surface SEM images of black and red tiger obsidian

### Mechanical Characterization

Modulus and hardness values of the three obsidian samples along with artificial lime glass, which were obtained by nano-indentation technique, are shown in Table 3.4. In the case of the red tiger and pink obsidians, indents were made in both the red and the jet-black areas, respectively. There was small difference seen in the values of hardness and modulus of

three different obsidians. Figure 3.9 shows a typical load vs displacement graph taken for different obsidians. It was confirmed by nano indentation that the hardness of all the obsidians was greater as compared to the lime glass. Glass is considered as elastic substance and, thus, can be characterized through a modulus of elasticity. This modulus increases as the lengthening at a certain applied stress diminishes. With increasing  $Al_2O_3$  content in the composition of glass, the structure becomes more rigid and the modulus of elasticity increases.

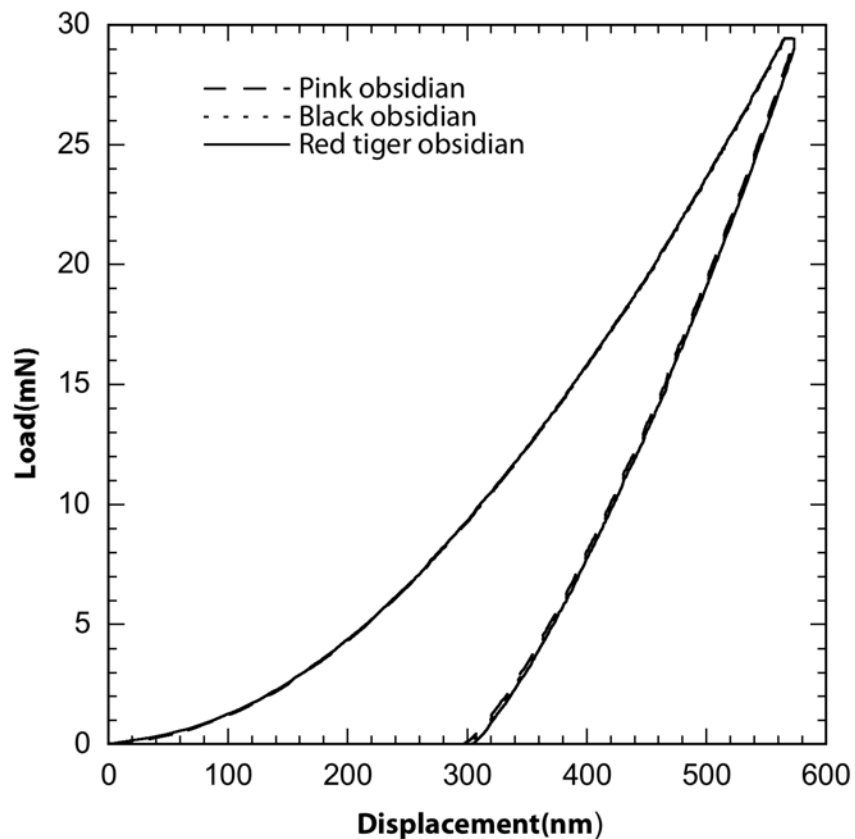


Figure 3.9: Typical load-displacement graph of nano indentation of obsidian

The rule of mixtures and inverse rule of mixtures was used to compare the elastic modulus of obsidian with artificial glass [52]. The rule of mixtures predicts that an upper limit of the elastic modulus of the composite is given in terms of the elastic moduli of the matrix ( $E_m$ ) and the particulate ( $E_p$ ) phases. Mechanical properties of composites are a combination of those of the components.

<b>Material</b>	<b>Modulus <math>\pm</math>Std Dev(GPa)</b>	<b>Hardness<math>\pm</math> Std dev(GPa)</b>
Black obsidian	61.2 $\pm$ 1.1	7.6 $\pm$ 1.3
Red tiger obsidian	56.9 $\pm$ 0.6	6.82 $\pm$ 1.0
Pink obsidian	60.8 $\pm$ 0.4	8.0 $\pm$ 1.2
Soda lime glass	44.1 $\pm$ 0.5	4.6 $\pm$ 0.1

Table 3.4: Nano-indentation on obsidian and artificial glass

$$E_c = E_m V_m + E_p V_p \quad (3.3)$$

where  $V_m$  and  $V_p$  are the volume fractions of the two phases. In the transverse direction on the assumption that particulate, matrix, and composite experience equal stresses, the Young modulus in tension can be estimated as follows:

$$E_t = \frac{E_m E_p}{E_p V_m + E_m V_p} \quad (3.4)$$

<b>Composition</b>	<b>Lime glass</b>	<b>Obsidian</b>	<b>Fused quartz</b>
SiO <sub>2</sub>	73	79.26	75.94
Na <sub>2</sub> O	14	4.14	0.7
CaO	7	0.35	0.4
Al <sub>2</sub> O <sub>3</sub>	2	12.41	14
K <sub>2</sub> O	-	3.98	0.6
Fe <sub>2</sub> O <sub>3</sub>	-	1.47	0.2
MgO	4	0.05	0.1
TiO <sub>2</sub>	-	0.11	1.1

Table 3.5: Chemical composition of obsidian and soda lime glass wt (%) [53]

The elastic modulus of obsidian and soda lime glass was calculated by using individual elastic moduli of each oxide in the material. As shown in the Table 3.6, the values of

elastic modulus are higher than the values that are found using nano-indentation method. This clearly suggests that the structure of the materials plays a role in their mechanical property. From the Table 3.6, in all the experiments, we can see the elastic modulus values for obsidian is greater than the artificial glass.

<b>Method</b>	<b>Obsidian</b>	<b>Soda lime glass</b>	<b>Fused quartz</b>
	E(GPa)	E(GPa)	E(GPa)
Pulse echo	67.5	52.87	-
Nano indentation	60.3	44.2	-
Rule of mixtures	78	71.5	80.4
Inverse rule of mixtures	67	62.5	78.1

Table 3.6: Comparison of elastic modulus using four different methods

For the ring on ring test, the stress calculated using Eqn. 2.6 is the maximum stress achieved by the sample with  $\sigma_{\text{RoR}} = \sigma_r = \sigma_t$ . For precise breaking strength determination, the fracture must initiate from the uniformly stressed region (the region within the central ring in RoR). This also defines the validity of the test where the failure must initiate from the central loaded region.

As shown in Fig. 3.10, the obsidian samples and the fused quartz show a valid failure pattern as per ASTM 1499. The validity of these tests were also identified by looking at the fracture, which originated from inside the loading ring instead of initiating beneath the ring. Figure 3.11 shows the typical loading curve obtained for the RoR biaxial tests done on the prepared discs. It shows medium strength failure for obsidian samples while high strength failure in case of fused quartz. The flexural strength results are shown in Fig. 3.7. All the strength values for fused quartz are higher than obsidian, but the strength values of red tiger obsidian was more closer to fused quartz.

The values of the fracture toughness measured by the SEVNB methods are given in Table 3.8. These values are the mean values of fracture toughness from a number of ex-

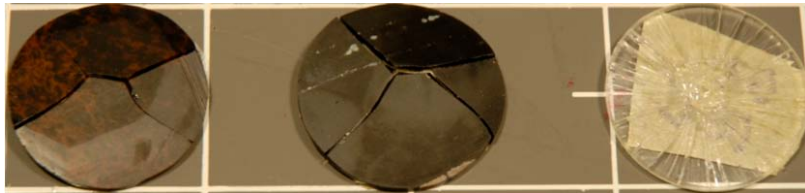


Figure 3.10: Typical ring-on-ring (RoR) failure of black, red tiger and fused quartz.

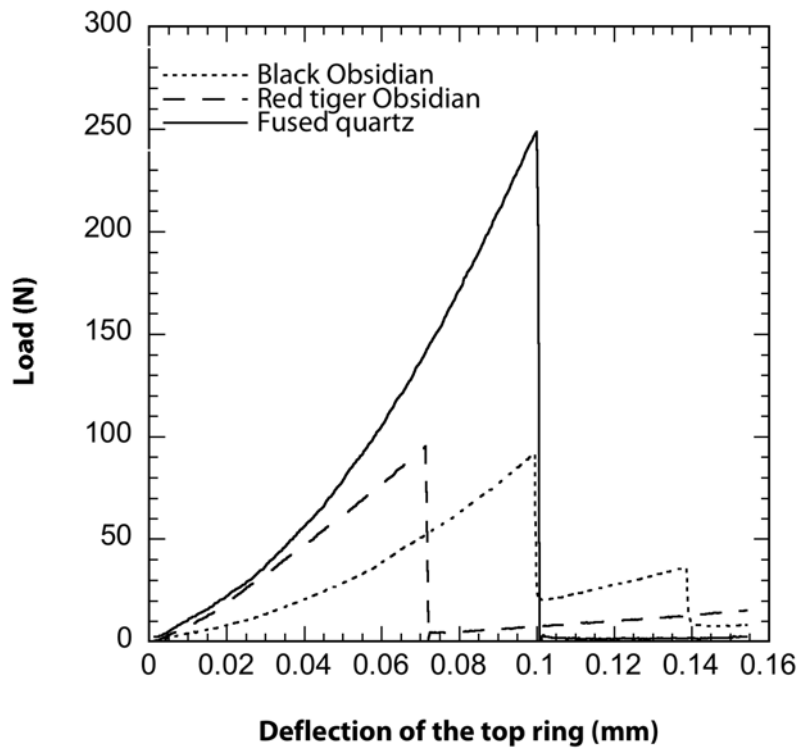


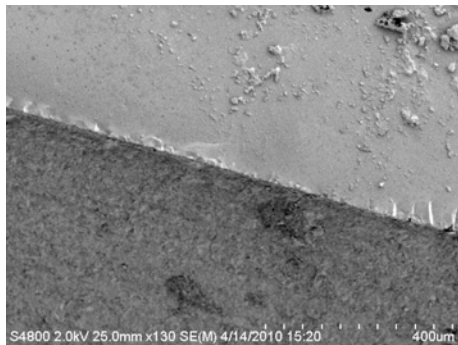
Figure 3.11: Typical load-deflection curve of obsidian under ring-on-ring (RoR).

Material	Biaxial strength $\pm$ Std Dev(MPa)
Black obsidian	$35 \pm 6.7$
Red tiger obsidian	$56.9 \pm 11.2$
Fused quartz	$100 \pm 32$

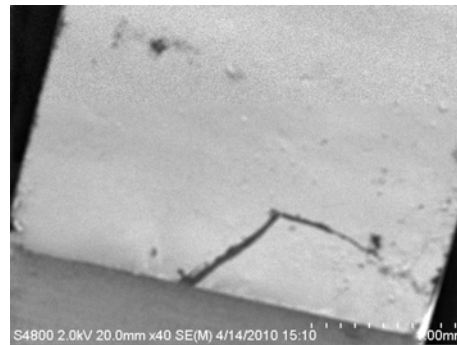
Table 3.7: Biaxial strength of black, red tiger and fused quartz.

periments. The table also, includes the mean values of the fracture toughness for quartz and artificial glass from literature. Awaji *et.al.* in his paper discussed that the values found SEVNB are lower than those by the SEPB. It is known that alumina has rising R-curve behavior, especially coarse-grained alumina because of interlocking on the precracked surface. For alumina, SEVNB method is a better method to estimate the fracture toughness. There is a significant amount of alumina in obsidian composition. Due to this, SEVNB is acceptable method to calculate the fracture toughness of obsidian.

SEM images of the fracture surface of obsidian are shown in Fig. 3.12. Figure 3.12(a) is the SEM image in the vicinity of the tip of the notch. It shows that the crack was propagated from the tip of the notch. Figure 3.12(b) shows flat surfaces that are characteristic of brittle fracture and there are striation formed along the crack length. This might be due to some inclusions silica, silicates or foreign compounds which might be present in the structure of obsidian.



(a) SEM fracture image of red tiger obsidian



(b) SEM fracture image of black obsidian

Figure 3.12: Scanning electron microscope(SEM) images of fracture surfaces of black and red tiger obsidian

<b>Sample</b>	<b>Fracture toughness (MPa <math>\sqrt{m}</math>)</b>
Black obsidian	1.31
Red tiger obsidian	1.28
Fused quartz	0.64
Artificial glass	0.58

Table 3.8: Values of fracture toughness measured by single edge V notch beam (SEVNB).

## CHAPTER 4

### CONCLUSIONS AND FUTURE WORK

Comparative examination of micro-mechanical features by combined Ring on Ring (ROR), single edge V notch beam (SEVNB) and nano-indentation tests reveals the strongly distinctive behavior of obsidian versus various kinds of artificial glass, including common lime glass, as well as fused quartz. The nano-indentation results show that the hardness for all the obsidians is significantly greater than that for common glass. Furthermore, the obsidian superior particularities in structure mechanics are reflected in almost all aspects such as fracture pattern, elastic modulus, hardness and fracture toughness.

The structure, morphology and chemistry of the three obsidians and all reference samples were comparatively investigated. Morphologically, all three obsidians particularly show hierarchical arrangement of inclusion networks in the amorphous matrix. The composition of obsidian show significant amount of alumina in all examined samples. Although the exact role of the alumina content in mechanics of obsidian is unclear, aluminum-containing silicate is well known for its good mechanical property. Indeed, an explicit correlation was found between unique mechanical particularities of obsidian and inhomogeneous hierarchical structure associated with segregation of its major chemical components, especially Si and O.

There are a few things which can be addressed to further understand the fracture mechanics of obsidian's more clearly.

- The initiation and progression of local failure processes during nanoindentation induced fracture can be characterized by monitoring of acoustic emission activity.
- The physical and mechanical properties of obsidian can be determined by studying

the true structure in detail

- To find the qualitative and quantitative information regarding highly localized failure events in obsidian, acoustic emission technique should be employed.

## **BIBLIOGRAPHY**

- [1] J.E. Ericson, A. Makishima, J.D. Mackenzie and R. Berger, "Chemical and physical properties of obsidian: A naturally occurring glass," *Journal of Non-Crystalline Solids* 17 (1975) 129-142.
- [2] L. E. Morgan, P. R. Renne, R.E. Taylor and G. WoldeGabriel, "Archaeological age constraints from extrusion ages of obsidian: Examples from the Middle Awash, Ethiopia," *Quaternary Geochronology* 4 (2009) 193-203.
- [3] L. Anthony and M. Neri, "Philippine obsidian and its archeological applications," *Indo-Pacific Prehistory Association Bulletin* 27, 2007.
- [4] J. Scherrer, "The Last of the Obsidian Artifacts in Puerto Vallarta," - Global Press Release Distribution, Nov 28, 2008.
- [5] L. Bellot-Gurlet, O. Doriguel and G. Poupeau, "Obsidian provenance studies in Colombia and Ecuador: obsidian sources revisited," *Journal of Archaeological Science* 35 (2008) 272-289. M. D. Glascock, *Obsidian Provenance Research in the Americas*, *Acc. Chem. Res.* 2002, 35, 611-617.
- [6] "Department of Earth Sciences, University College London," [www.es.ucl.ac.uk/schools/Glossary/obsidian.htm](http://www.es.ucl.ac.uk/schools/Glossary/obsidian.htm), retrieved on 05/12/2010.
- [7] M.L. Moss and J.E. Erlandson, "The Archeology of obsidian Cove, Sumez Iseland, Southeast, Alaska," *Arctic Anthropology* Vol. 38, No. 1 PP. 27-47, 2001.
- [8] F. L. Bourdonnec, J. M. Bontempi, N. Marini, S. Mazet, P. F. Neuville, G. Poupeau and J. Sicurani, "SEM-EDS characterization of western Mediterranean obsidians and

- the Neolithic site of A Fuata (Corsica),” *Journal of Archaeological Science* 37 (2010) 92-106.
- [9] M. D. Glascock, *Obsidian Provenance Research in the Americas*, *Acc. Chem. Res.* 2002, 35, 611-617.
- [10] A. J. Nazaroff, K. M. Prufer and B. L. Drake, “Assessing the applicability of portable X-ray fluorescence spectrometry for obsidian provenance research in the Maya lowlands,” *Journal of Archaeological Science* 37 (2010) 885-895.
- [11] G. R. Summerhayes, “Obsidian Network Patterns in Malanesia-Sources, characterization a Distribution,” *Ippa Bulletin* 29, 2009: 109-123.
- [12] C. S. Smith, “Obsidian Use in Wyoming and the concept of Curation ,” *Plains Anthropologist*, Aug 1999, 44, 169, *Research Library*, 271.
- [13] C. MA, G. R. Rossman, J. A. Miller “The Origion of Color in Fire Obsidian,” *The Canadian Mineralogist* Vol. 45, pp. 551-557 (2007).
- [14] Cann, J.R., and A.C. Renfrew, “The Characterization of Obsidian and its Application to the Mediterranean Region,” *proceedings of the Prehistoric Society* 30, 111-133.
- [15] A. I. Dalakishvili, “Glass Formation in Perlite- and Obsidian-Containing Batches,” *Glass Physics and Chemistry*, Vol. 31, No. 6, 2005, pp. 820-822.
- [16] A. Derkowiski, “Experimental Transformation of Volcanic Glass from Streda Nad Bologom (Selovakia),” *Institute of geological Sciences*.
- [17] A. Negash and M. S. Shackley, “Geochemical Provenance of Obsidian Artifacts from the MSA site of Proc Epic Ethiopia,” *Archaeometry* 48, 1 (2006) 1-12.
- [18] A. Negash, M. Alene, F.H. Brown, B.P. Nash and M.S. Shackley, “Geochemical sources for the terminal Pleistocene/early Holocene obsidian artifacts of the site of Beseka, central Ethiopia,” *Journal of Archaeological Science* 34 (2007) 1205-1210.

- [19] B. Logan, R. E. Huges, and D. H. Henning, "Western Oneota Obsidian: Sources and implication," *Plains Anthropologists*, Vol. 46, No. 175, PP. 55-64, 2001.
- [20] H. B. Abdelounisa, K. Elleuch, R. Vargiolu, H. Zahouani and A. Le Bot, "On the behaviour of obsidian under scratch test," *Wear* 266 (2009) 621-626.
- [21] N. Agazi, M. S. Shackley, and Mulugeta Alene, "Source Provenance of Obsidian Artifacts from the Early Stone Age (ESA) Site of Melka Konture, Ethiopia," *Journal of Archaeological Science* 33:1647-1650.
- [22] N. Craig, R. J. Speakman, R. S. Popelka-Filcoff, M. Aldenderfer, L. F. Blanco, M. B. Vega, M. D. Glascock and C. Stanish, "Macusani obsidian from southern Peru: A characterization of its elemental composition with a demonstration of its ancient use," *Journal of Archaeological Science* 37 (2010) 569-576.
- [23] M. S. Shackley, "Archaeological Obsidian Studies: Method and Theory," *American Antiquity*, Vol. 64, No. 3 (Jul., 1999), pp. 560-561
- [24] N. Rani, J. P. Shrivastava, and R. K. Bajpai, "Obsidian: a potential natural analogue for nuclear waste glass," *Current Science*, Vol. 98, No. 7, 10 April, 2010.
- [25] B. F. Dorfman, L. C. Zhang, and R. P. Singh, "Distinguished Mechanical Behavior of Volcanic Glasses versus Artificial Glasses," *Journal of the American Ceramic Society*.
- [26] M. Oddone, G. Bigazzi, Y. Keheyan and S. Meloni, "Characterization of American obsidians: Implications for raw material supply for prehistoric artifacts," *Journal of Radioanalytical and Nuclear Chemistry*, Vol. 243, No. 32000) 673-682.
- [27] P. Rzsá, Z. Elekes, A. Simon, J. Simulák, I. Uzonyi and Z. Kiss, "Phenocrysts in obsidian glasses," *Journal of Radioanalytical and Nuclear Chemistry*, Vol. 256, No. 2 (2003) 329-337.

- [28] M. S. Shackley, "Obsidian: Geology and Archaeology in the North American Southwest," *Geoarchaeology: An International Journal*, Vol. 22, No. 8, 935-949 (2007).
- [29] P. Dyjak and R.P. Singh, "Acoustic Emission Analysis of Nanoindentation-Induced Fracture Events," *Experimental Mechanics* (2006) 46: 333-345.
- [30] A. K. Singh, "Novel Fabrication of SiC Based Ceramics for Nuclear Application," dissertation Doctor of Philosophy, May 2009.
- [31] "Measurement of Elastic Constants Using Ultrasound," MCEN 3027, 02/26/2001, <http://www.panametrics.com/ndt/theory/>
- [32] "Sound propagation in solids," 3B Scientific GmbH, Rudorffweg 8, 21031 Hamburg, Germany, [www.3bscientific.com](http://www.3bscientific.com)
- [33] R. Rai'utis, L. Ma'eika, R. Ka'ys and A. Vladi'auskas, "Application of the ultrasonic pulseecho technique for quality control of the multilayered electronic components," ISSN 1392-2114 *Ultragarsas (Ultrasound)*, Vol.62, No.3, 2007.
- [34] E. A. Ginzl and R.K. Ginzl, "Ultrasonic Properties of A new Low Attenuation dry Couplant Elastomer" Ginzl Brothers and Associates Ltd. April 1994.
- [35] J. Mirbagher, M. Tajvidi, I. Ghasemi and J. C. Hermanson, "Prediction of the Elastic Modulus of Wood Flour/Kenaf Fibre/Polypropylene Hybrid Composites," *Iranian Polymer Journal* 16 (4), 2007, 271-278.
- [36] H. Stanjek and W. Hausler, "Basics of X-ray Diffraction," *Hyperfine Interactions* 154: 107119, 2004.
- [37] W. C. Oliver and G. M. Pharr, "An improved technique for determining hardness and elastic modulus using load and displacement sensing indentation experiments," *J. Mater. Res.*, Vol. 7, No. 6, June 1992.

- [38] W.C. Oliver and G.M. Pharr, "Measurement of hardness and elastic modulus by instrumented indentation: Advances in understanding and refinements to methodology," *J. Mater. Res.*, Vol. 19, No. 1, Jan 2004
- [39] M. F. doerner and W. D. Nix, "A Method for interpreting the data from Depth-sensing indentation instruments," *J. Mater Res.* 1(4) Jul/Aug 1986.
- [40] S. V. Hainsworth, H. W. Chandler,a) and T. F. Page, "Analysis of nanoindentation load-displacement loading curves," *J. Mater. Res.*, Vol. 11, No. 8, Aug 1996.
- [41] L. Calabri N. Pugno and S. Valeri, "AFM Nanoindentation Method: Geometrical Effects of the Indenter Tip,"
- [42] T. Fett, G. Rizzi, J. P. Guin and S. M. Wiederhorn, "Ring-on-ring strength measurements on rectangular glass slides," *J Mater Sci* (2007) 42:393-395.
- [43] L. Ceriolo and A. Di Tommaso, "Fracture Mechanics of Brittle Materials: A Historical Point of View," 2nd Int. PhD Symposium in Civil Engineering 1998.
- [44] S. R. Choi , J. A. Salem and A. Chuly, "Analysis of Precracking Parameters and Fracture Toughness for Ceramic Single Edge Precracked Beam Specimens," NASA Technical Memorandum, August 1992.
- [45] J. J. Kruzic and R. O. Ritchie, "Determining the Toughness of Ceramics from Vickers Indentations Using the Crack-Opening Displacements: An Experimental Study," *J. Am. Ceram. Soc.*, 86 [8] 1433-36 (2003).
- [46] H. Awaji, T. Watanabe and Y. Sakaida, "Fracture Toughness Measurements of Ceramics by V Notch Technique," *Ceramics International* 18 (1992) 11-17.
- [47] M. M. Woo, "Empirical evaluation of fracture toughness: the toughness of quartz," *American Mineralogist*, Volume 67, pages 1065-1066, 1982.

- [48] A.T. Zlatkin and E.L. Lube, "Estimation of fracture toughness and residual stress in brittle crystals from indentation-induced acoustic emission," *Journal of Crystal Growth* 18 (1992) 218-231.
- [49] A. T. Zehnder, "Lecture Notes on Fracture Mechanics," Department of Theoretical and Applied Mechanics Cornell University, Ithaca, NY 14853, June 23, 2009.
- [50] I. M. Abdulagatov, S. N. Emirov, T. A. Tsomaeva, Kh. A. Gairbekov, S. Ya. Askerov and N. A. Magomedova, "Thermal conductivity of fused quartz and quartz ceramic at high temperatures and high pressures" *Journal of Physics and Chemistry of Solids* Volume 61, Issue 5, May 2000, Pages 779-787
- [51] ASTM, E1225-04, "Standard Test Method for Thermal Conductivity of Solids by Means of the Guarded-Comparative-Longitudinal Heat Flow Technique," in ASTM International.
- [52] K. K. Chawla, "On the Applicability of the 'Rule-of-Mixtures' to the Strength Properties of Metal-Matrix Composites," *Revista Brasileira de Física*, Vol. 4, No 3, 1974.
- [53] TED PELLA. INC., Microscopy Products for Science and Industry, Web Site: <http://www.tedpella.com>
- [54] ASTM, C1499-05. "Standard Test Method for Monotonic Equibiaxial Flexural Strength of Advanced Ceramics at Ambient Temperature".

## VITA

Mohammed S. Husien

Candidate for the Degree of  
Master of Science

Thesis: FRACTURE BEHAVIOR AND MECHANICAL CHARACTERIZATION OF  
OBSIDIAN: NATURALLY OCCURRING GLASS

Major Field: Mechanical Engineering

Biographical:

Personal Data: Born in Addis Ababa, Ethiopia on January 6, 1980.

Education:

Received the B.Sc. degree from Bahir Dar University, Bahir Dar, Ethiopia, 2004, in Mechanical Engineering.

Completed the requirements for the degree of Master of Science with a major in Mechanical Engineering Oklahoma State University in July, 2010.

Experience:

Worked as a Graduate Research Assistant at the Mechanics of Advanced Materials Laboratory headed by Dr. Raman P. Singh in the area of Ceramics.

Name: Mohammed S. Husien

Date of Degree: July, 2010

Institution: Oklahoma State University

Location: Stillwater, Oklahoma

Title of Study: FRACTURE BEHAVIOR AND MECHANICAL CHARACTERIZATION  
OF OBSIDIAN: NATURALLY OCCURRING GLASS

Pages in Study: 40

Candidate for the Degree of Master of Science

Major Field: Mechanical Engineering

Obsidian is a natural glass of volcanic origin that is formed by the rapid cooling of viscous lava. Obsidian is commonly assumed to possess a fracture behavior identical to that of artificial glass. This study is specifically concerned with mechanical properties and fracture behavior of obsidian. Nano-indentation techniques are used to study the hardness, modulus and fracture behavior of obsidian in comparison to some reference material samples. The indentation results indicated that obsidian's mechanical properties are better than anecdotally accepted values for obsidian. When compared to artificial glasses, such as fused quartz and soda lime glass, the crack propagation threshold of obsidian is higher. Analytical methods such as XRD, SEM and EDS are used in order to discover distinctive structural features of obsidian. The strength of obsidian samples is measured by ring-on-ring (RoR) test. The RoR configuration is the most acceptable form associated with an ASTM standard that provides the maximum area under a constant maximum stress. One of the primary areas of focus of this investigation is the determination of the fracture toughness of obsidian. Therefore, single edge V notched beam (SEVNB) method is used to find the fracture toughness value of obsidian. Specially made diamond slicing wheel is used to machine the V notch. The SEVNB specimens are loaded in three point bend flexure to the point of failure and the peak load is used to determine the fracture toughness. Further study on mechanical properties of obsidian may lead to new findings useful for various fields of material development. However, due to extreme complexity of mechanisms of formation and complicated obsidian structure, the further research needs cross-disciplinary efforts.

ADVISOR'S APPROVAL: \_\_\_\_\_